

Local structure of $\text{LiNi}_{0.5}\text{Mn}_{0.5}\text{O}_2$ cathode material probed by *in situ* x-ray absorption spectroscopy

Aniruddha Deb^{a)}

*Environmental Energy Technologies Division, Lawrence Berkeley National Laboratory,
One Cyclotron Road, Berkeley, California 94720*

Uwe Bergmann

Stanford Synchrotron Radiation Laboratory, Sand Hill Road, Menlo Park, California 94025

Stephen P. Cramer

*Physical Bioscience Division, Lawrence Berkeley National Laboratory, One Cyclotron Road, Berkeley,
California 94720 and Department of Applied Sciences, University of California, Davis, California 95616*

Elton J. Cairns

*Environmental Energy Technologies Division, Lawrence Berkeley National Laboratory,
One Cyclotron Road, Berkeley, California 94720 and Department of Chemical Engineering,
University of California, Berkeley, California 94720*

(Received 24 September 2005; accepted 27 January 2006; published online 16 March 2006)

The layered nickel manganese oxide of $\text{LiNi}_{0.5}\text{Mn}_{0.5}\text{O}_2$ is a technologically important and promising cathode material for lithium-ion batteries. A study of the structural perturbation, charge compensation mechanism, and the valence of the constituent transition metal elements (Ni and Mn) during electrochemical cycling was performed using x-ray absorption spectroscopy (XAS) employing an *in situ* technique with an electrochemical cell designed for long term x-ray experiments. We present the changes in the oxidation state, bond distance, and coordination number of the Ni and Mn absorbers as a function of the state of charge of the material during electrochemical cycling at moderate rate through a typical Li-ion battery operating voltage range (2.9–4.7 V). The oxidation states of the transition metals in $\text{LiNi}_{0.5}\text{Mn}_{0.5}\text{O}_2$ are Mn^{4+} and Ni^{2+} . The x-ray absorption near edge spectra reveal that on delithiation of $\text{Li}_{1-x}\text{Ni}_{0.5}\text{Mn}_{0.5}\text{O}_2$ the Mn is electrochemically inactive and remains at Mn^{4+} whereas the Ni is oxidized from Ni^{2+} to almost Ni^{4+} through an intermediate stage of Ni^{3+} . A quantitative picture of the Ni valence during the charging process was obtained employing Faraday's law calculations in combination with the XAS results. The Faraday's law calculation indicated that at the end of the charge Ni is at $\text{Ni}^{3.91+}$ in close agreement with the XAS results where Ni is found to be at $\text{Ni}^{3.88+}$ at the end of the charge. Analysis of the extended x-ray absorption fine structure shows that during cycling the material retains its crystallographic symmetry and good structural short-range order which should lead to stable cycling. © 2006 American Institute of Physics. [DOI: 10.1063/1.2179198]

I. INTRODUCTION

Lithium manganese oxides have been of great interest technologically for their application in advanced lithium-ion batteries.^{1–3} These materials include $\text{Li}_{(2/3)+x}(\text{Ni}_{1/3}\text{Mn}_{2/3})\text{O}_2$ (where $x=0$ or $1/3$) with the layered O_2 structure which exhibits a reversible capacity of ~ 180 mAh/g in the voltage range of 2.5–4.5 V (vs Li).^{4,5} Stable 4 V performance has been observed for the layered $\text{LiNi}_{0.5}\text{Mn}_{0.5}\text{O}_2$,^{6,7} $\text{Li}(\text{Ni}_{1/3}\text{Co}_{1/3}\text{Mn}_{1/3})\text{O}_2$,^{8,9} and $\text{Li}(\text{Ni}_x\text{Co}_{1-2x}\text{Mn}_x)\text{O}_2$ ($x \leq 0.5$).^{10,11} These layered compounds are isostructural to LiCoO_2 (with α - NaFeO_2 or O_3 structure). Of these, $\text{LiNi}_{0.5}\text{Mn}_{0.5}\text{O}_2$ is a very attractive material^{6,12} as a possible alternative 4 V cathode material to the presently used LiCoO_2 in Li-ion batteries. Ohzuku and Makimura¹³ showed that lithium manganese oxide represents a possible alternative to LiCoO_2 for advanced Li batteries, in terms of its

operating voltage, capacity, cyclability, and safety. Furthermore, the high cost of cobalt metal and its toxicity create an incentive for efforts to find viable alternative oxide materials. The LiNiO_2 also exhibits a large capacity and good rate capability but unfortunately shows a high reactivity with organic electrolytes and instability in its layered structure at high voltage above 4.5 V which may result in a battery hazard on overcharge or under other abuse conditions, hence failing to replace LiCoO_2 as a commercially viable cathode material.¹⁴ LiMn_2O_4 , another candidate for replacing LiCoO_2 , exhibits good structural stability on overcharge but has low capacity and high solubility as Mn^{2+} in the electrolyte at elevated temperatures above 55 °C.¹⁵ Considering the merits of LiNiO_2 and LiMn_2O_4 , the synthesis and the study of the characteristics of layered $\text{LiNi}_{1-x}\text{Mn}_x\text{O}_2$ has recently drawn interest. Rossen *et al.*¹⁶ observed that an increase of the Mn content led to cation mixing of Li and transition metal ions resulting in a low cell capacity, while later, Spahr *et al.*¹⁷ reported the synthesis of phase-pure $\text{LiNi}_{1-x}\text{Mn}_x\text{O}_2$ by using the Mn and Ni hydroxides, coprecipitated from LiOH

^{a)} Author to whom correspondence should be addressed; present address: Stanford Synchrotron Radiation Laboratory (SSRL), 2575 Sand Hill Road, Menlo Park, CA 94025; electronic mail: adeb@slac.stanford.edu

solution. For $\text{LiNi}_{0.5}\text{Mn}_{0.5}\text{O}_2$, the initial capacity was about 170 mAh/g but the cyclability was very poor. A reversible capacity of 150 mAh/g (2.5–4.3 V) was observed by Ohzuku and Makimura¹³ and 150 mAh/g (3.0–4.4 V) by Lu *et al.*^{6,7} Furthermore, Kim *et al.*¹⁸ studied the stable cycling performance of the solid solution of $x\text{Li}(\text{Ni}_{1/2}\text{Mn}_{1/2})\text{O}_2 \cdot (1-x)\text{Li}_2\text{TiO}_3$ ($x=0.05$). These materials have been attractive not only because of their high reversible capacity but also due to the absence of Co, which makes it more cost effective and less toxic. The x-ray absorption near-edge structure (XANES) study on this solid solution revealed that the Ni is in the Ni^{2+} state.¹ Our recent study on the similar layered material $\text{Li}(\text{Ni}_{1/3}\text{Co}_{1/3}\text{Mn}_{1/3})\text{O}_2$ confirmed the involvement of the $\text{Ni}^{2+} \leftrightarrow \text{Ni}^{3+} \leftrightarrow \text{Ni}^{4+}$ redox couple in the 2.7–4 V region.¹⁹ The potential for increased stability and improved electrochemical performance by $\text{Li}(\text{Ni}_{0.5}\text{Mn}_{0.5})\text{O}_2$ is still being investigated. Hence an *in situ* x-ray absorption spectroscopic study of this material during cycling will be of importance and will directly help us to probe and understand the stability and the electrochemical performance during the charge-discharge cycling of this system.

There has been a continuous effort to study the detailed changes that occur in various electrode materials during the charge-discharge process. In the case of modern Li-ion batteries, the electrode material permits the lithiation and delithiation, a process that in the long run can lead to degradation of the electrodes severely limiting the lifetime of the battery. Hence a real time tracking of the structure and valence changes during cycling can be illuminating and can be achieved by employing an in-situ electrochemical cell. The x-ray absorption spectroscopy (XAS), accompanied by simultaneous electrochemical measurements, provides valuable and important information about the relationship between the structure and electrochemical properties, information that is not accessible utilizing *ex situ* experimental measurements.

Recently, the oxidation process in $\text{LiNi}_{0.5}\text{Mn}_{0.5}\text{O}_2$ cathode material was studied by Yoon *et al.*,²⁰ where they suggested by utilizing modeling that Li-deintercalation involves the $\text{Ni}^{2+} \leftrightarrow \text{Ni}^{3+} \leftrightarrow \text{Ni}^{4+}$ redox couple, but there was no direct experimental observation at a certain state of charge (SOC) that the intermediate Ni^{3+} state is present during the charging cycle which is very important to understand the electrochemical changes during the ongoing reaction in the 2.7–4.0 V region. In this study, we here first report the direct experimental evidence of the intermediate state of Ni^{3+} (at 55% SOC), during the first charging cycle as discussed in the following section. In this study, we utilize the transmission XAS to investigate the $\text{LiNi}_{0.5}\text{Mn}_{0.5}\text{O}_2$ cathode material in the various stages of charge and discharge during electrochemical cycling. Utilizing the *in situ* technique XAS offers the possibility of monitoring the structural and electronic changes during an ongoing electrochemical process. The XANES region of the *K*-absorption edge of the transition metal elements (Ni and Mn) was used to obtain information about their valence states and electronic configurations, while the extended X-ray absorption fine structure (EXAFS) region was utilized to probe the changes in structure around the x-ray absorbing atoms. Recently, the characterization and

analysis of this promising material were performed in the *ex situ* mode utilizing the x-ray diffraction (XRD) and x-ray photoelectron spectroscopy (XPS) methods.^{21,22} It is important to note here that in contrast to XRD which gives one a good picture of the long-range structural changes in the cathode material, *in situ* XAS investigations during cycling are very illuminating in their own right, providing an understanding of the oxidation state as well as short-range ordering, and a baseline for further studies in which the electrode material is modified by the introduction of additional elements. Furthermore, XAS can distinguish between the bulk properties (measurement in transmission mode) and surface properties (by fluorescence, or even more restricted to surface by electron yield, or grazing incidence measurements). Here, in this investigation, we present a comprehensive analysis of the Ni and Mn *K*-edge EXAFS, as well as the analysis of XANES. We also correlate the XAS information to the electrochemical measurements and calculations.

II. EXPERIMENTAL PROCEDURES

A. $\text{LiNi}_{0.5}\text{Mn}_{0.5}\text{O}_2$ electrode and electrochemical XAS cell assembly

The experiments were performed using a complete Li/ $\text{LiNi}_{0.5}\text{Mn}_{0.5}\text{O}_2$ cell. The layered compound prepared was first verified to be single phase using XRD. The electrodes used in the *in situ* cell were fabricated from an intimate mixture of $\text{LiNi}_{0.5}\text{Mn}_{0.5}\text{O}_2$ powder that is comprised of 80% by the weight of the total electrode with 10% polyvinylidene difluoride polymer binder (Kynar), 10% compressed acetylene black in *N*-methyl-2-pyrrolidinone (NMP). The NMP was then evaporated at 60 °C for 6 h and finally the electrodes were dried at 120 °C for another 6 h. The thickness of the active mass on the electrode was about 200 μm . For a complete description of the design and the assembly of the electrochemical *in situ* cell, the reader is referred to Ref. 23. The *in situ* cell was assembled in a glove box. Celgard 3400 membrane was used as a separator and 1 M LiPF_6 in ethylene carbonate (EC)+diethyl carbonate (DEC) (1:1 volume, Merck, LP40) as the electrolyte. The Li metal foil cut into a circular disk (10 mm diameter) was used as the counter electrode. The charge-discharge cycling and cyclic voltammetry were performed at room temperature at the beam line with a potentiostat/galvanostat system (Princeton Applied Research, Model Versa) under constant current control.

The electrochemical cycling was performed at a constant current density of 0.4 mA/cm² between 2.5 and 4.7 V, which corresponds to about the 6 h rate, as shown in Fig. 1. The *in situ* measurements were performed at various SOC during the charge and discharge. For the measurements with the model compounds, the samples were diluted with boron nitride (BN) (samples were mixed in a 1:10 ratio with BN using a mortar and pestle), and 0.8 cm² pellets were prepared. The sample pellets were then finally loaded on aluminum holders using the Kapton adhesive foil on both sides of the sample.

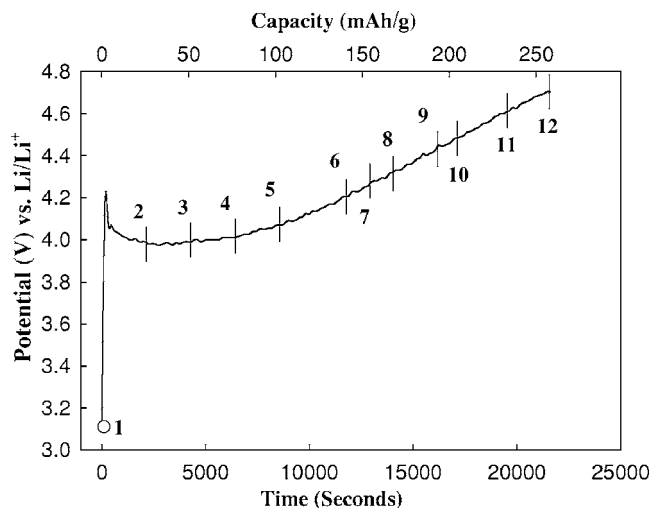


FIG. 1. Voltage profile of the XAS *in situ* electrochemical cell during the first charge. The XAS scans are measured at the points indicated in the voltage profile.

B. X-ray absorption spectroscopy measurement and data analysis

The XAS measurements were performed in the transmission mode at the bending magnet beamline station D of the DND-CAT (Sector 5), at the Advanced Photon Source, using a water cooled Si(111) double crystal monochromator and the energy resolution of the monochromatic beam was determined to be ~ 1.0 eV. A beam size of about 0.3×0.5 mm² was used for the beam to pass easily through the in-situ cell x-ray window resulting in an incident photon flux of $\sim 10^{10}$ photons/s. The monochromator was scanned in energy from 200 eV below to 800 eV above the Mn and Ni *K*-absorption edges (6539 and 8333 eV). Data were collected in this energy range, with a step size of 0.2 eV in the respective edge regions. The energy calibrations were performed using Mn and Ni metal foils between the I_t and the I_{ref} ion chambers, respectively.

The EXAFS data analysis was performed using the standard procedure using the EXAFSPAK software package²⁴ and Athena.²⁵ The measured absorption spectrum below the preedge region was fitted to a straight line. The background contribution above the postedge region, $\mu_0(E)$, was fitted to a fourth order polynomial. The fitted polynomials were extrapolated through the total energy region and subtracted from the total absorption spectra. The background subtracted spectra were then normalized for the above energy region. The normalized $\chi(E)$ spectra were converted to $\chi(k)$ in the k space [$(k = 8\pi^2 m(E - E_0)/h^2)^{1/2}$]. The resulting $\chi(k)$ function was then weighted with k^3 to account for the damping of oscillations with increasing k . The radial structure function was then obtained by Fourier transform (FT) of the normalized k^3 -weighted EXAFS spectra, $k^3\chi(k)$, using a k range of 2.0–15.2 Å⁻¹ for Mn and Ni.

III. RESULTS AND DISCUSSION

A. Structure of LiNi_{0.5}Mn_{0.5}O₂

The structure of LiNi_{0.5}Mn_{0.5}O₂ has been previously studied by different groups.²² Our XRD investigation of the

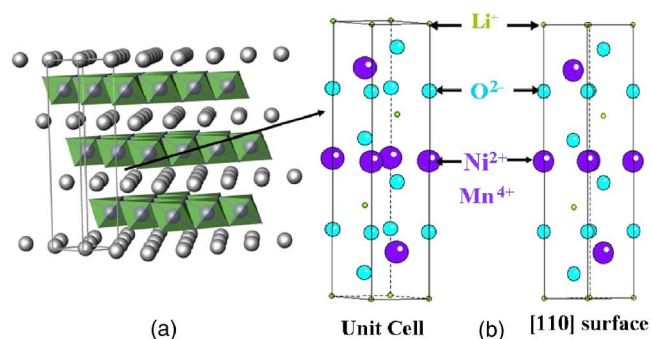


FIG. 2. (Color online) (a) Hexagonal layered structure (α -NaFeO₂-type) of LiNi_{0.5}Mn_{0.5}O₂ with a space group of $R\bar{3}m$. (b) Shows the unit cell and the atomic arrangements along the [110] surface.

LiNi_{0.5}Mn_{0.5}O₂ electrode revealed a typical XRD pattern similar to that of the LiNiO₂, as reported earlier by Kobayashi *et al.*²⁶ The XRD patterns can be indexed on the basis of the α -NaFeO₂-type structure, space group $R\bar{3}m$, ITC #166 (International Tables for X-ray Crystallography). The hexagonal layered $R\bar{3}m$ structure of the LiNi_{0.5}Mn_{0.5}O₂ is shown in Fig. 2. The lattice parameters of our sample were consistent with the earlier reported values.²² In this structure, the Li ions are at the $3a(0,0,0)$ sites whereas the transition metals M ($M = \text{Ni}$ and Mn) are at the $3b(0,0,0.5)$ sites and the oxygen ions are the $6c(0,0,z)$ sites in a hexagonal setting. While it is important to mention here that a partial interchange in occupancy between the Li and the transition metal sites (i.e., with Li in the $3b$ sites and M in the $3a$ sites) leads to disordering in the structure called “cation mixing” which is seen to cause a deterioration in the electrochemical performance of this kind of layered compounds.^{27,28} Recently, theoretical first principle calculations²⁹ on this material revealed that the average Mn–O bond (~ 1.93 Å) length hardly varies with the variation of the Li concentration while the Ni–O bond length varies dramatically by about 0.15 Å with the change in the Li content. For the delithiated sample, the Ni–O bond length was found to be about 1.90 Å. With the delithiation, the decrease in the cell volume in this material is smaller ($\sim 3\%$),³⁰ in contrast to the large decrease in the cell volume for other transition metal oxides such as LiNiO₂ ($\sim 10\%$), LiMnO₂ ($\sim 8\%$), and LiCoO₂ ($\sim 6\%$). This small change in the cell volume is very beneficial with respect to the cycling stability, cell life, and rate capability.

B. XAS results for LiNi_{0.5}Mn_{0.5}O₂

1. XANES

LiNi_{0.5}Mn_{0.5}O₂ has a hexagonally layered structure and during charging it undergoes a phase change from one type of hexagonal structure to another hexagonal structure with a shorter a axis and a longer c axis which is similar to that observed in the case of LiNiO₂ cathode material. But unlike LiNi_{0.5}Mn_{0.5}O₂, LiNiO₂ undergoes an additional transition to a third hexagonal phase with a much shorter c axis, as verified by *in situ* XRD measurements.³⁰ To elucidate the charge compensation mechanism in this system, Mn and Ni *K*-edge XAS experiments were carried out during the charge up to the nearly fully charged state (~ 259 mAh/g) at a constant

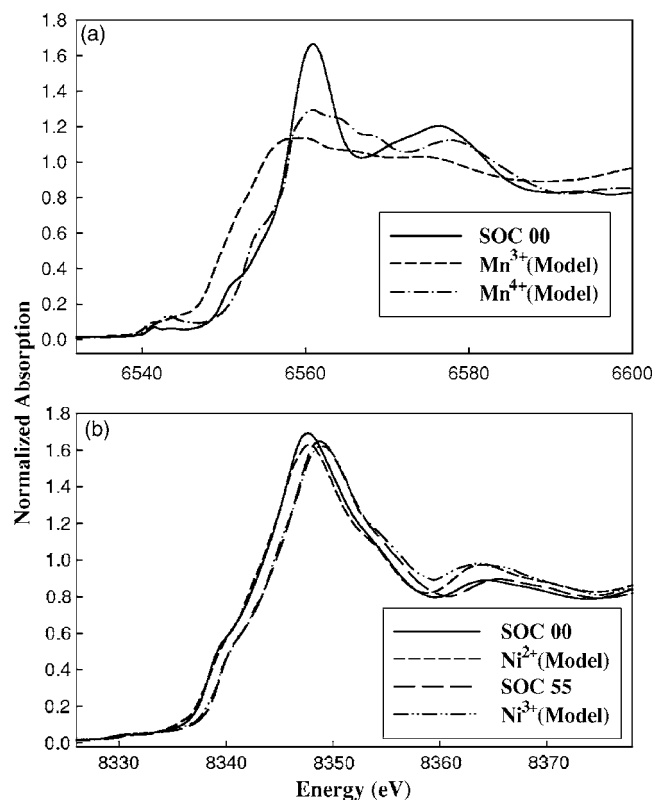


FIG. 3. Calibrated and normalized XANES comparison of (a) Mn *K* edge for $\text{LiNi}_{0.5}\text{Mn}_{0.5}\text{O}_2$, observed at 0% SOC with the model compounds Mn_2O_3 (Mn^{3+}) [broken line] and MnO_2 (Mn^{4+}) [dash-dot line]. (b) Ni *K* edge for $\text{LiNi}_{0.5}\text{Mn}_{0.5}\text{O}_2$, observed at 0% SOC [thick-solid line] and 55% SOC [thick-broken line] with the model compounds Nickel (II) oxide (Ni^{2+}) [broken line] and $\text{LiNi}_{0.8}\text{Co}_{0.2}\text{O}_2$ (Ni^{3+}) [dash-dot-dot line], respectively.

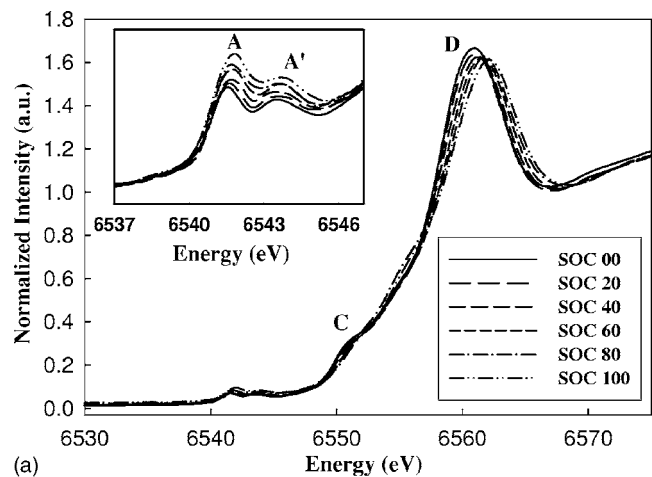
current density of 0.4 mA/cm^2 ($\sim 41 \text{ mA/g}$). The voltage profile of the *in situ* electrochemical cell during the first charge for experiments performed at the Mn and the Ni *K* edges is shown in Fig. 1. The specific capacity was calculated from the elapsed time, current, and the mass of the active material in the cathode, assuming that all the current passed was due to the Li deintercalation. Generally, the shape of the *K*-edge XANES of the transition metal oxides exhibits unique information about the site symmetry and the nature of the bonding with the surrounding ligands, while the threshold energy position of the absorption edge provides a valuable information about the oxidation state of the probed atom. To obtain the information about the oxidation state of the Mn and the Ni atoms in this sample, we compared the Mn and the Ni *K*-edge XANES of $\text{LiNi}_{0.5}\text{Mn}_{0.5}\text{O}_2$ with those of the model compounds. The comparison of the XANES region at the 0% SOC with that of the model compounds is shown in Fig. 3. In Fig. 3(a) the Mn *K*-edge XANES spectrum of $\text{LiNi}_{0.5}\text{Mn}_{0.5}\text{O}_2$, when compared with the model compounds Mn_2O_3 (Mn^{3+}) and MnO_2 (Mn^{4+}), reveals that the edge energy is identical to that of MnO_2 (Mn^{4+}), clearly indicating the oxidation state of Mn in $\text{LiNi}_{0.5}\text{Mn}_{0.5}\text{O}_2$ is tetravalent (i.e., Mn^{4+}). Figure 3(b) shows the comparison of the Ni *K*-edge XANES spectrum with those of the model compounds Nickel (II) oxide [NiO (Ni^{2+})] and layered $\text{LiNi}_{0.8}\text{Co}_{0.2}\text{O}_2$ (Ni^{3+}). At 0% SOC, the XANES of the Ni *K* edge is similar to that of the Nickel (II) oxide, indicating that

the Ni in $\text{LiNi}_{0.5}\text{Mn}_{0.5}\text{O}_2$ is divalent (i.e., Ni^{2+}) whereas the Ni *K*-edge XANES spectrum of the layered $\text{LiNi}_{0.8}\text{Co}_{0.2}\text{O}_2$ is similar to that observed at 55% SOC, confirming that in $\text{LiNi}_{0.5}\text{Mn}_{0.5}\text{O}_2$, Ni is in the trivalent state (i.e., Ni^{3+}) at 55% SOC (1 Li removed per Ni atom).

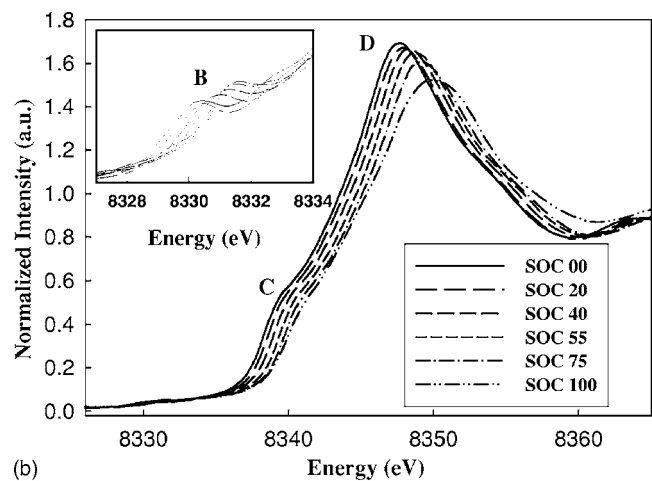
Figure 4 shows the XANES spectra for the selected SOC values at the Mn and Ni edges, respectively. The metal *K*-edge XANES spectra originate from transitions of the $1s$ core electron of the transition metal to excited vacant states with appropriate symmetry. For the Mn *K*-edge XANES [Fig. 4(a)], during charge, the edge position of the scans at different states of charge did not exhibit any significant edge shift to higher energies, suggesting that the Mn oxidation state remains unchanged during the charging procedure, i.e., the Mn^{4+} atom is electrochemically inactive. The Ni *K*-edge XANES [Fig. 4(b)] exhibits a two stage reaction during the charging process. The first stage is from 0% SOC to 55% SOC while the second stage is from 55% SOC to 100% SOC. This two stage observation can be attributed to the valence change of almost two for the Ni ions ($\text{Ni}^{2+}/\text{Ni}^{3+}$ and $\text{Ni}^{3+}/\text{Ni}^{4+}$) during charging. This kind of two step reaction was reported recently by Reed and Ceder,²⁹ utilizing the first principle quantum mechanical energy calculations, indicating that the redox reaction in $\text{Li}_{1-x}\text{Ni}_{0.5}\text{Mn}_{0.5}\text{O}_2$ consists of $\text{Ni}^{2+}/\text{Ni}^{3+}$ and $\text{Ni}^{3+}/\text{Ni}^{4+}$, respectively. In their work, the Ni redox reaction takes place in the ranges of $0 \leq x \leq 0.5$, $0.5 \leq x \leq 1$, respectively. Thus our experimental observation is consistent with these calculations except for the fact that we observe the Ni^{3+} at $x=0.48$ as shown in Fig. 5 instead of $x=0.5$ as obtained in the calculations. This difference is within the experimental error. During discharge, these processes are reversed electrochemically: Li is inserted in the lattice, Ni^{4+} is reduced to Ni^{2+} (divalent) and *M* (Metal)–O and M–M bond lengths return to their original values. Hence, we have presented only the data during the charging cycle.

It is important to note here that the shapes of the absorption edges for Ni in the various states of charge cannot be represented by linear combinations of the Ni^{4+} and Ni^{2+} edges. For example, Fig. 4(c) shows a comparison of the spectrum calculated by linear combination of the Ni^{2+} and Ni^{4+} spectra and the spectrum for 55% SOC. The important areas of mismatch are the concave downward feature at 8340 eV, and the absorption maximum. The feature at 8340 eV is characteristic of Ni^{3+} , and is absent from the calculated edge spectrum; the mismatch in the absorption maximum is an additional indication of the presence of Ni^{3+} instead of a combination of Ni^{2+} and Ni^{4+} . This is a strong evidence for the existence of Ni^{3+} as an intermediate state for the Ni in its oxidation/reduction cycling.

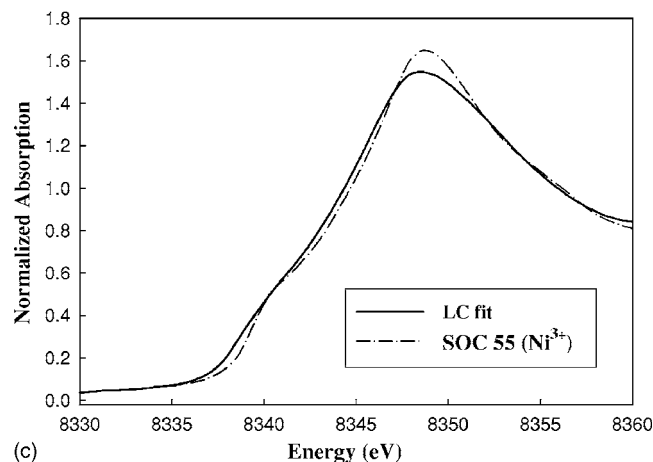
The insets of Figs. 4(a) and 4(b) show the nature of the preedge peaks of the respective XAS spectra. The preedge peak provides additional information about the nature of the electronic states. For many transition metals, the preedge peaks occur well below the main edge ($\sim 15 \text{ eV}$ below) and are assigned to transitions to empty states with *d*-like character,^{31,32} i.e., these are $1s$ to $3d^{(n+1)}$ transitions where *n* is the initial number of *d* electrons and (*n*+1) includes the excited electron in the final state, which generally includes the effect of the core hole. The weak preedge absorption



(a)



(b)



(c)

FIG. 4. Calibrated and normalized XANES spectra for $\text{LiNi}_{0.5}\text{Mn}_{0.5}\text{O}_2$ at different states of charge at the (a) Mn K edge (0% SOC, 20% SOC, 40% SOC, 60% SOC, 80% SOC, and 100% SOC) (b) Ni K edge (0% SOC, 20% SOC, 40% SOC, 55% SOC, 75% SOC, and 100% SOC). The inset, shows the nature of the pre-edge peaks of the respective XAS spectra. (c) Comparison of the linear combination (LC) fit of the Ni^{2+} (SOC 00) and Ni^{4+} (SOC 100) spectra [with a composition of 46% SOC 00 and 54% SOC 100 states] with the SOC 55 spectra.

which exhibits peaks A and A' (near 6542 and 6544 eV), is the formally electric dipole-forbidden transition of a $1s$ electron to an unoccupied $3d$ orbital of a high spin ($t_{2g}^3 e_g^0$) Mn^{4+} ion, which is partially allowed because of the pure electric quadrupole coupling and/or the $3d$ - $4p$ (or Mn $3d$ -O $2p$) or-

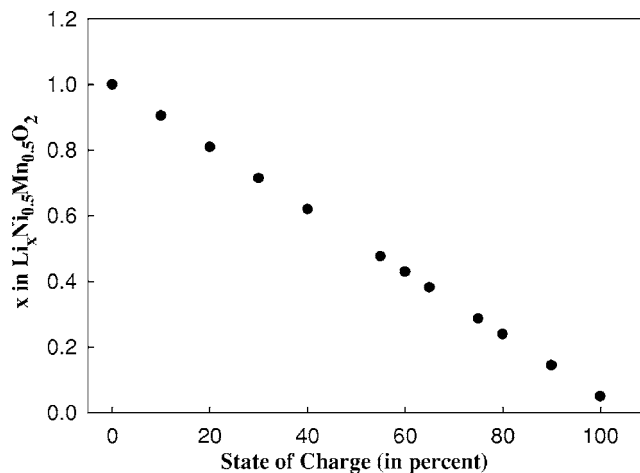


FIG. 5. The Li-deintercalation (x) from $\text{Li}_x\text{Ni}_{0.5}\text{Mn}_{0.5}\text{O}_2$ with respect to the state of charge during the first charging cycle.

bital mixing arising from the noncentrosymmetric environment of the slightly distorted octahedral $3a$ site in the rhombohedral $R\bar{3}m$ space group. Experimentally, the quadrupole nature of the $1s \rightarrow 3d$ pre-edge feature in D_{4h} CuCl_4^{2-} was demonstrated by Hahn *et al.*³³ along with the analysis of the angular dependence of the $1s \rightarrow 3d$ transition intensity, utilizing polarized synchrotron radiation, and oriented single crystals. The weak pre-edge intensity is indicative of octahedral coordination as opposed to tetrahedral coordination which results in a strong pre-edge intensity.³⁴ It is now well established that the shape and the position of the pre-edge peaks are related to the oxidation state of the absorbing ion and local arrangement of the backscattering ions, respectively. The two peaks in the pre-edge region for Mn are discernable as Mn is in the tetravalent state (Mn^{4+}), since a single peak in the pre-edge region is the characteristic of trivalent (Mn^{3+}) Mn compounds. This latter single peak characteristic of trivalent manganese compounds can be explained as splitting of the t_{2g} and e_g energy levels modified by the Jahn-Teller distortion.³⁵ For Ni as shown in Fig. 4(b) [inset] the pre-edge is very weak. In the octahedral Ni(II) complexes only the $1s \rightarrow e_g$ transition are possible, and furthermore this $1s \rightarrow e_g$ transition is symmetry forbidden for the centrosymmetric pointgroups.³⁶ This signifies that highly symmetrical octahedral complexes will not exhibit any pre-edge peaks, while nonsymmetrical octahedral complexes can be detected by their higher $1s \rightarrow 3d$ peak intensity. Hence, the intensity of the $1s \rightarrow 3d$ peak can be used as an indicator of the geometry in the octahedral complexes. In Fig. 4(b) the presence of the very weak $1s \rightarrow 3d$ transition pre-edge leads to the conclusion that the local environment of the Ni atoms is not highly symmetrical, instead the weak pre-edge is due to the slight distortion of the octahedral $3a$ site in the rhombohedral $R\bar{3}m$ space group, which results in the removal of the inversion symmetry. Figure 6 shows the variations of the pre-edge peak positions for the Mn and Ni K -edge XANES in this system during charging. It is clearly evident that the peak position of the pre-edge in the Ni K -edge XANES moves toward higher energy during the charging process, reflecting the increase of the oxidation state of the Ni ion in the system. In contrast, the peak positions of the pre-edge peaks in the

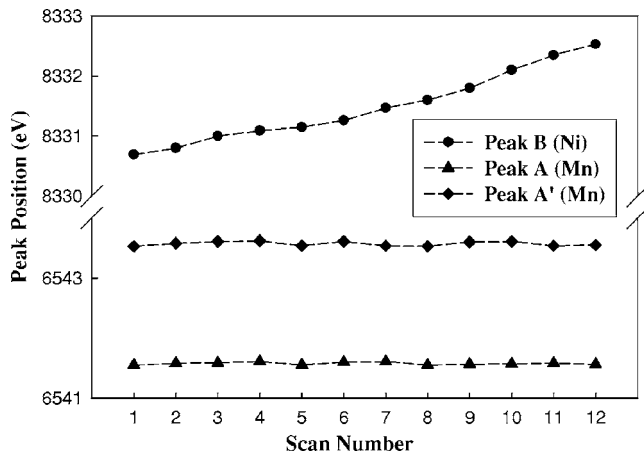


FIG. 6. Variations of the preedge peak position for the Mn and the Ni K edge XANES of $\text{LiNi}_{0.5}\text{Mn}_{0.5}\text{O}_2$ during the charging at a constant current density.

Mn K -edge XANES do not exhibit any substantial change during the charging process, further supporting the fact that the manganese in the system is electrochemically inactive and remains tetravalent (Mn^{4+}). The shoulder in the absorption spectra, peak C in Fig. 4, (~ 8338 eV for Ni and ~ 6552 eV for Mn) is attributed to the $1s \rightarrow 4p$ transition and a shakedown transition due to the ligand-to-metal charge transfer (LMCT) and has been previously identified by Yoon *et al.*²⁰ as a LMCT shakedown process. This kind of peak has been observed for other transition metal compounds such as $\text{Dy}_{1-x}\text{Ca}_x\text{CoO}_3$ (Ref. 37) or $\text{La}_{1-x}\text{Sr}_x\text{CoO}_3$,³⁸ where it was shown that the LMCT state $t_{2g}^6 e_g^1 L^1$ contributes to about 45% to the ground state.

From Fig. 4(a), it is evident that as the Li ion is deintercalated, the Mn XANES spectrum shows some changes as regards to the shape of the edge due to the change in the local environment of the Mn in the system, but does not exhibit any rigid shift to higher energies. Thus, it shows clear evidence that Mn in $\text{LiNi}_{0.5}\text{Mn}_{0.5}\text{O}_2$ is electrochemically inactive and the oxidation state remains tetravalent (Mn^{4+}), and is not oxidized as a result of the Li deintercalation during the charging process. In contrast, the Ni edge shifts to higher energies on charging. The entire edge shifts to the higher energy region indicating that the average oxidation state of nickel ions increases during charging. As was shown earlier (Fig. 3) the charging process is a two step reaction, at the beginning of the charging process (at 0% SOC) Ni ions in $\text{LiNi}_{0.5}\text{Mn}_{0.5}\text{O}_2$ are divalent (Ni^{2+}), at 55% SOC the Ni ions in the system are trivalent (Ni^{3+}), and finally at 100% SOC the Ni ion oxidation state reaches close to tetravalent (Ni^{4+}) (as will be shown later in this section).

In order to present a quantitative picture of how the oxidation process is taking place in this system, we present in Fig. 7 a plot of the white line peak position as a function of the SOC, as opposed to the edge position, as defined by the energy at half of the edge step for the Ni K edge, observed during delithiation (charge) and lithiation (discharge). For the Ni metal centers, the change in the peak position is about 3.1 eV, as the lithium content changes from the open circuit voltage (OCV) fully discharged state to the fully charged

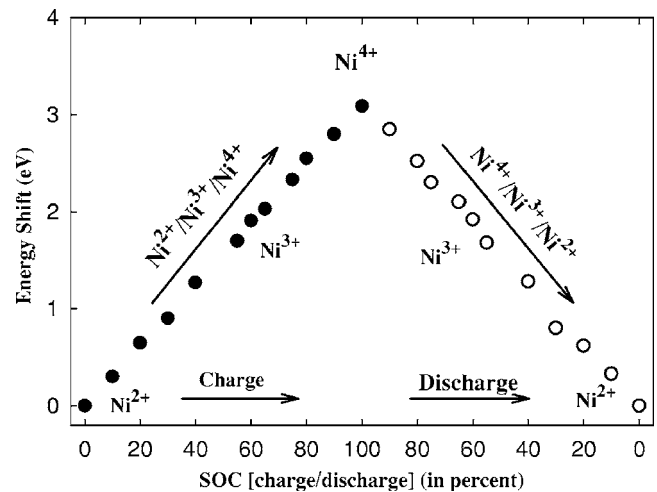
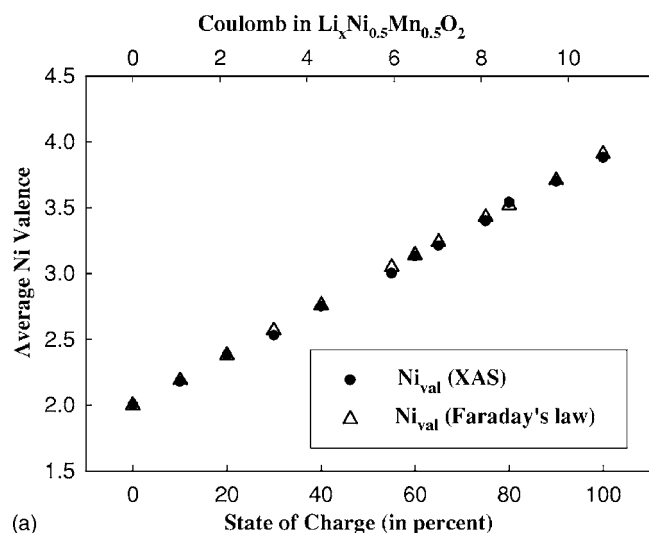


FIG. 7. Plot of the white line energy shift vs the state of charge (SOC), for the Ni K edge. The filled symbol (\bullet) represents the data during the charge (i.e., during delithiation), while the empty symbol (\circ) represents the data during discharge (i.e., lithiation).

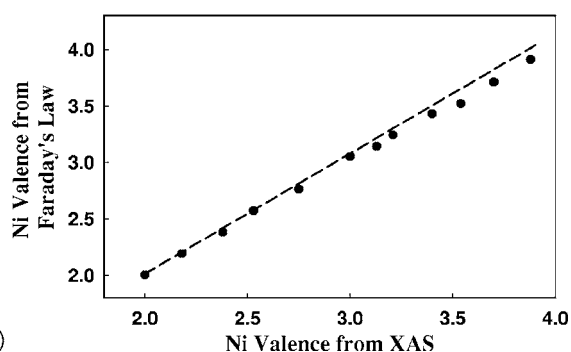
(4.7 V vs Li) state. From the figure it is evident that the Ni oxidation state changes smoothly (consistent with the Faraday's law calculation, which will be discussed later in this section), showing that the oxidation process consists of two stages (from 0% SOC to 55% SOC and from 55% SOC to 100% SOC), which is due to the two-electron reaction of Ni as discussed in the earlier section. In contrast to the previous work by Yoon *et al.*,²⁰ where there was no quantitative analysis to establish the relationship between the amount of Li extracted and the valence of the Ni during the ongoing electrochemical reaction here we present a further qualitative and quantitative pictures of the valence change during the charging cycle (with respect to the state of charge) of the constituent transition metals in this system, here we combined the information from the XAS results and the electrochemistry utilizing Faraday's law. Utilizing this approach helped us to relate directly the redox changes of the constituent elements (Ni and Mn) in the system with the electrochemical state at each individual SOC. This helps us to clearly see how the Li deintercalation and intercalation during charging and discharging in this cathode material led to the changes of the white lines and the interatomic distances in this material. Using Faraday's law, the theoretical capacity of $\text{LiNi}_{0.5}\text{Mn}_{0.5}\text{O}_2$ is 280 mAh/g (for Ni^{2+} being converted to Ni^{4+}). So theoretically for the average valence change of Ni ($\text{Ni}^{2+} - \text{Ni}^{3+}$, $\text{Ni}^{3+} - \text{Ni}^{4+}$, and Mn is electrochemically inactive and stays at Mn^{4+} during the full charging cycle) in this compound, the capacity used for a Ni valence change of one will be a half of the total theoretical capacity, i.e., 140 mAh/g. Hence utilizing the experimentally measured capacity at each state of charge in the charging process and the theoretical capacity, we can represent the average Ni valence during the charging cycle as

$$Ni_{\text{val}}(\text{average}) = 2.0 + \left[\frac{\text{Exp. measured charge (mAh/g)}}{140(\text{mAh/g})} \right]. \quad (1)$$

Then using the above equation (1) we can find the Ni average valence at different SOC. We can then compare the re-



(a)



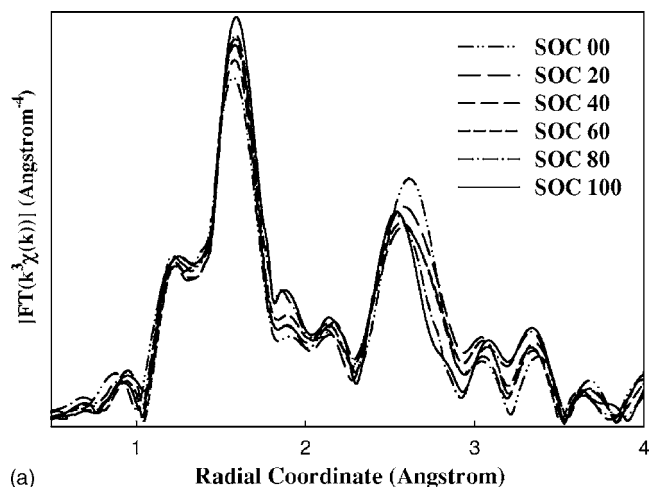
(b)

FIG. 8. (a) Comparison of the average valence vs SOC/coulomb profiles for the first charge of the cell for the transition metal Ni, from the Faraday's law calculation (Δ) and XAS results (\bullet). (b) Plot of the Ni average valence from XAS results vs the Faraday's law calculations. The dashed line is the guide using the Faraday's law showing how the Ni valence should change during the first charging cycle.

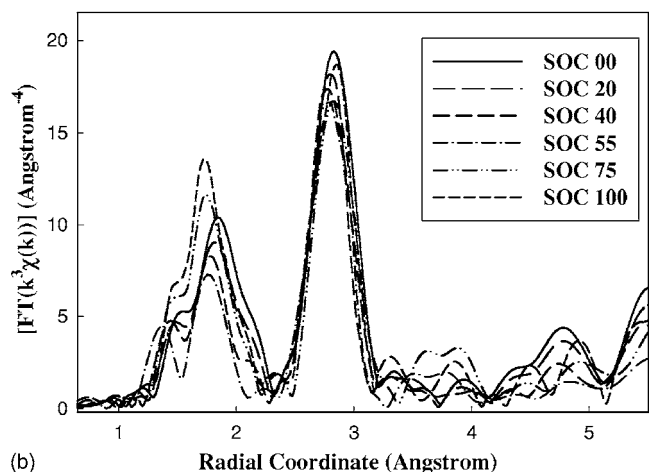
sults from the Faraday's law calculation and that obtained from the XAS results. The quantitative information and comparison of the average Ni valence between the Faraday's law calculation and the XAS results are shown in Fig. 8, where we can see that during the first charge [Fig. 8(a)] cycle Ni is changed from Ni^{2+} to $\text{Ni}^{3.88+}$, close to Ni^{4+} . The dashed line in Fig. 8(b) shows the comparison of the results for the Ni valence state from the Faraday's law calculation and the results based on the white line energy shift. The agreement is within the experimental error.

2. EXAFS during the first charging cycle

The local structure of the Mn and Ni ions in $\text{LiNi}_{0.5}\text{Mn}_{0.5}\text{O}_2$ was measured by EXAFS. Figure 9 shows the Fourier transform magnitudes of the Mn and Ni *K*-edge EXAFS spectra during the first charging cycle. The first coordination shell consists of oxygen, while the peak feature arising due to the second coordination shell is mainly dominated by the manganese and the nickel cations. Here in this study, the scattering by the Li atom is neglected as the back-scattering amplitude of the photoelectron due to the scattering by Li is very weak. The most significant change during charge is observed in the first coordination shell around the Ni atoms. The dramatic changes of the first coordination



(a)



(b)

FIG. 9. Selected k^3 -weighted Fourier transform magnitudes of the EXAFS spectra of $\text{Li}_x\text{Ni}_{0.5}\text{Mn}_{0.5}\text{O}_2$ (a) at the Mn *K* edge and (b) Ni *K* edge during the charge cycle [k range=2.0–15.2 Å].

peaks during charge directly indicates that charge compensation mainly occurs at the Ni sites and hence results in a significant decrease in the average Ni–O bond distances. During charge, it is seen that the Mn–O distances remains nearly unchanged, in contrast to the decrease of the Ni–O distances. These variations of the interatomic distances are closely related or can be attributed to the change in the valence state in transition metals. In the presence of an octahedral crystal field, d orbitals split into triply degenerate (t_{2g}) and a higher energy doubly degenerate set (e_g). Hence the outermost configuration of $\text{Ni}^{2+}/\text{Ni}^{4+}$ (or $\text{Ni}^{3+}/\text{Ni}^{4+}$) can be represented as $t_{2g}^6e_g^2/t_{2g}^6e_g^0$ (or $t_{2g}^6e_g^1/t_{2g}^6e_g^0$). Thus during the oxidation reaction of the charging cycle, the change in energy for $\text{Ni}^{2+}/\text{Ni}^{4+}$ (or $\text{Ni}^{3+}/\text{Ni}^{4+}$) would be larger as the change takes place between the lower t_{2g} and the higher e_g sets, inducing a larger change in ionic radius ($R_{\text{Ni}^{2+}} \sim 0.69 \text{ \AA}/R_{\text{Ni}^{3+}} \sim 0.56 \text{ \AA}/R_{\text{Ni}^{4+}} \sim 0.48 \text{ \AA}$). It is important to note here that during delithiation from 0% SOC to 55% SOC the amplitude of the Ni–O peak decreases but from 55% SOC to 100% SOC the amplitude of Ni–O peak increases. These observations can be best understood by considering the local structure of Ni in pure LiNiO_2 . As observed earlier for LiNiO_2 (Ref. 39) oxygen atoms are present at two different distances surrounding Ni. This distorted octahedral coord-

TABLE I. Structural parameters from the curve-fitting results for the first two peaks of the Fourier-transform $k^3\chi(k)$ at the Mn K edge at different states of charge (SOC). The SOC (in percent), shell (Z_a-Z_b), Coordination number (CN), bond distance (R), and Debye-Waller disorder (σ^2) are tabulated. The coordination number (CN) of both Mn-O and Mn-M contributions were constrained to be six. The number in the parentheses is the uncertainty in last digit or digits of the parameter.

SOC (%)	Z_a-Z_b	CN	R (Å)	σ^2 ($\text{Å}^2 \cdot 10^{-3}$)
00	Mn-O	6	1.971 (5)	3.5 (6)
	Mn-M	5.3 (5)	2.935 (5)	3.9 (7)
20	Mn-O	6	1.967 (4)	3.6 (6)
	Mn-M	5.3 (5)	2.929 (6)	4.1 (6)
40	Mn-O	6	1.961 (5)	3.5 (5)
	Mn-M	5.3 (5)	2.920 (6)	4.2 (5)
60	Mn-O	6	1.956 (5)	4.3 (6)
	Mn-M	5.3 (5)	2.903 (6)	4.8 (7)
80	Mn-O	6	1.955 (5)	4.6 (6)
	Mn-M	5.3 (5)	2.893 (6)	5.0 (6)
100	Mn-O	6	1.951 (5)	4.3 (4)
	Mn-M	5.3 (5)	2.888 (4)	4.1 (5)

dination is consistent with Jahn-Teller effect expected for Ni^{3+} in a low spin state. During delithiation, the increase in Ni-O peak amplitude has been attributed to the changes in the local structure of the Ni created by the oxidation of the Ni^{3+} to Ni^{4+} . Since Ni^{4+} is not the Jahn-Teller active ion; the oxidation of Ni^{3+} to Ni^{4+} results in a diminution of the Jahn-Teller effect which results in an increased amplitude of the Ni-O peak. Thus based on these observations, it is understood in this system during delithiation from 55% SOC to 100% SOC (when Ni is oxidized from Ni^{3+} to Ni^{4+}) a diminution of the Jahn-Teller effect results in an increased amplitude of the Ni-O peak. On the contrary from 0% SOC to 55% SOC (when Ni is oxidized from Ni^{2+} to Ni^{3+}) increase of the Jahn-Teller effect results in a decrease of amplitude of the Ni-O peak.

The second peak in Fig. 9 corresponds to the metal-metal interaction. It is seen that there is some change in the M - M (metal) peak position. For both Mn and Ni, the M - M peaks shifts to lower R values as Li is deintercalated. In pure LiNiO_2 a similar behavior has been observed by Nakai and Kagome⁴⁰ for the Ni-Ni interaction.

Quantitative analysis to obtain the EXAFS structural parameters for both Mn and Ni was performed by fitting the first two peaks of the FT spectra at the K edges of Mn and Ni, respectively, in $\text{LiNi}_{0.5}\text{Mn}_{0.5}\text{O}_2$. The structural parameters obtained by the curve fitting are summarized in Table I and II, respectively. The coordination number (CN) of Ni-M was fitted for all SOC with the constraint that the CN remains same during charge. The local structure of the Mn environment during the start of the charge contains six oxygen atoms at ~ 1.971 Å. Contrary to the first coordination shell, the coordination number of the second shell at ~ 2.94 Å is $\sim 5.3 \pm 0.5$, which is less than the calculated CN of 6 based on the nominal composition of $\text{LiNi}_{0.5}\text{Mn}_{0.5}\text{O}_2$ material. This observation is consistent with the earlier studies of x-ray refinement for a similar material,^{6,41} where the presence of disordering was observed between Li^+ and Ni^{2+} ,

TABLE II. Structural parameters from the curve-fitting results for the first two peaks of the Fourier-transform $k^3\chi(k)$ at the Ni K edge at different states of charge (SOC). The SOC (in percent), shell (Z_a-Z_b), Coordination number (CN), bond distance (R), and Debye-Waller disorder (σ^2) are tabulated. The coordination number (CN) of both Mn-O and Mn-M contributions were constrained to be six. The number in the parentheses is the uncertainty in last digit or digits of the parameter.

SOC (%)	Z_a-Z_b	CN	R (Å)	σ^2 ($\text{Å}^2 \cdot 10^{-3}$)
00	Ni-O	6	2.070 (4)	4.6 (5)
	Ni-M	6	2.925 (6)	4.9 (6)
20	Ni-O	6	2.038 (5)	4.1 (8)
	Ni-M	6	2.919 (5)	5.1 (6)
40	Ni-O	3.5 (3)	1.925 (3)	4.7 (7)
	Ni-O	2.5 (3)	2.127 (3)	5.5 (5)
	Ni-M	6	2.902 (5)	5.6 (5)
55	Ni-O	4.2 (2)	1.918 (3)	4.8 (8)
	Ni-O	1.8 (2)	2.082 (4)	4.8 (8)
75	Ni-O	6	2.894 (5)	6.1 (6)
	Ni-M	6	1.961 (4)	4.1 (6)
100	Ni-O	6	2.889 (5)	5.6 (5)
	Ni-O	6	1.894 (3)	4.5 (4)
	Ni-M	6	2.874 (4)	4.9 (5)

which was due to the similar radius of the Ni^{2+} (0.69 Å) and Li^+ (0.76 Å) cations. The first shell Mn-O and Ni-O interatomic distances at various charge and discharge states are shown in Fig. 10. It is evident from the results that during the charge the Mn-O distances varied by only a small amount (0.02 Å). The local structure of the Ni environment during the start of the charge contains 6.0 atoms at ~ 2.07 Å, while at 55% SOC the Ni environment is best represented by a long bond at 2.08 Å and a short bond at 1.92 Å and the end of the charge the Ni environment shows 6.0 atoms at ~ 1.89 Å, respectively. For the octahedrally coordinated compounds it has been previously seen that the Ni-O distances are very similar, where the Ni^{2+} -O bond length is about 2.07 Å, Ni^{3+} exhibiting a static Jahn-Teller distortion shows Ni^{3+} -O long bond at ~ 2.06 Å and a short bond at ~ 1.90 Å, finally the Ni^{4+} -O bond length is ~ 1.88 Å,

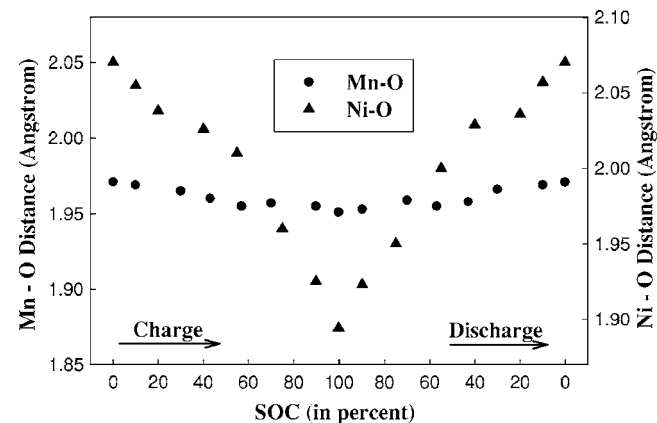


FIG. 10. First shell metal-oxygen bond length changes during $\text{Li}/\text{Li}_x\text{Ni}_{0.5}\text{Mn}_{0.5}\text{O}_2$ cell cycling. The filled symbols (● and ▲) represent the Mn-O and Ni-O bond distances as observed during different states of charge and discharge. At 40% and 55% SOC the points represent the average Ni-O bond distances.

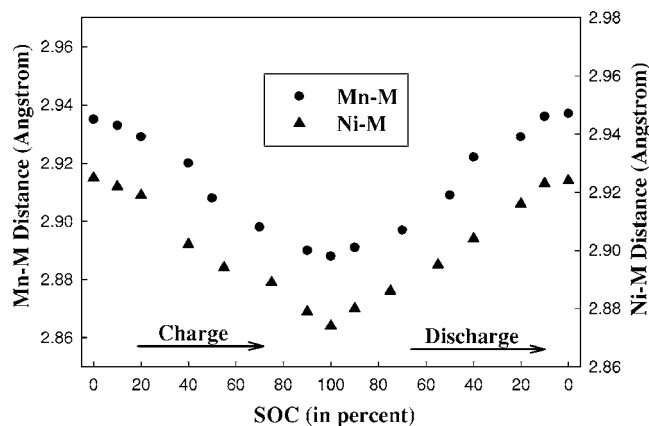


FIG. 11. Second shell metal-metal bond length changes during $\text{Li}/\text{Li}_x\text{Ni}_{0.5}\text{Mn}_{0.5}\text{O}_2$ cell cycling. The filled symbols (● and ▲) represent the Mn–M and Ni–M bond distances as observed at different states of charge and discharge.

respectively.^{42,43} Hence the fit results suggest that the average oxidation state of Ni ion at start of the charge is Ni^{2+} , while at 55% SOC it is Ni^{3+} and finally at the end of the charge Ni ion is close to the Ni^{4+} . In contrast to Mn–O, the significant change in the Ni–O bond length can be explained by the oxidation of Ni^{2+} – Ni^{4+} since the ionic radius of Ni^{2+} (0.69 Å) is larger than that of Ni^{4+} (0.46 Å).⁴⁴ Furthermore, the Ni^{4+} –O bond distance in this system (1.89 Å) is consistent with other previously reported Ni^{4+} –O bond distances observed in compounds such as BaNiO_3 and KNiO_6 (~1.88 Å).^{45,46} This also indicates that at the end of the charge Ni^{2+} is oxidized close to Ni^{4+} . Finally, the second shell metal-metal (Mn–M and Ni–M) interaction distances at various charge and discharge states are shown in Fig. 11. It is interesting to note that the change in the M–M distances at the Mn and Ni K edges between the initial and fully charged state varies at the most by 0.05 Å, about 1.7% contraction. These metal-metal distances correspond to the *a* lattice parameter of the trigonal *R*-3*m* cell. Contraction of this metal-metal distances observed here in this system are consistent with the observation of x-ray diffraction pattern for a similar system $\text{Li}_x\text{Ni}_{1/3}\text{Co}_{1/3}\text{Mn}_{1/3}\text{O}_2$.⁴⁷

IV. CONCLUSIONS

In situ Mn and Ni K-edge XAS characterizations for the layered $\text{LiNi}_{0.5}\text{Mn}_{0.5}\text{O}_2$ cathode material have been performed during the first charge and discharge process. XAFS has provided us with an excellent tool for analyzing the changes that occur when Li is cycled in and out of the layered lattice of $\text{Li}_{1-x}\text{Ni}_{0.5}\text{Mn}_{0.5}\text{O}_2$ in a Li-ion battery. Observation of the Mn and the Ni K-edge XANES results, confirms that the charge compensation during cycling (charge and discharge) is achieved mainly by the oxidation/reduction of Ni^{2+} , Ni^{3+} , and Ni^{4+} ions, while Mn remains unchanged in the Mn^{4+} oxidation state and is electrochemically inactive. We have shown, by direct experimental evidence, that in this system the oxidation process takes place in two steps, Ni^{2+} – Ni^{3+} and Ni^{3+} – Ni^{4+} which is also consistent with our Faraday's law results. The Faraday's law calculation along with the XAS results most importantly show that at the end

of the charge (4.7 V vs Li/Li^+) Ni is at $\text{Ni}^{3.88+}$ and is close to Ni^{4+} and not exactly Ni^{4+} which has been predicted by most of the earlier studies. The EXAFS results confirm the presence of Ni^{2+} ions at the start of the charge where the Ni–O bond length is ~2.07 Å, while at the end of charge the Ni–O bond distance is ~1.89 Å consistent with what is expected for a Ni^{4+} –O bond. There are three types of evidence for the existence of Ni^{3+} : the absorption edge for the mid-SOC composition is not a linear combination of the edges for Ni^{2+} and Ni^{4+} , the static Jahn-Teller effect illustrated in Fig. 9(b), and the Ni–O bond lengths in the mid-SOC region.

The observed shrinkage of the M–M distances is ~1.7% during the cycling process which scales with the *a* lattice parameter, is consistent with that observed in other similar layered compounds. These small changes in interatomic distances and the absence of any phase change indicate that this material is a promising candidate for a positive electrode material for use in rechargeable lithium cells.

ACKNOWLEDGMENTS

We thank Dr. M. Doeff of the Materials Science Division, Lawrence Berkeley National Laboratory for supplying us with the $\text{LiNi}_{0.5}\text{Mn}_{0.5}\text{O}_2$ cathode material. The XAS measurements were performed at the DND-CAT beamline at APS which is supported by the E. I. DuPont de Nemours & Co., The Dow Chemical Company, the U. S. National Science Foundation through Grant No. DMR-9304725 and the State of Illinois through the Department of Commerce and the Board of Higher Education Grant No. IBHE HECA NWU 96. This work was supported by the Director, Office of Basic Energy Sciences, Chemical Sciences Division of the U. S. Department of Energy, under Contract No. DE-AC03-76SF00098. Use of the Advanced Photon Source was supported by the U. S. Department of Energy, Office of Science, Office of Basic Energy Sciences, under Contract No. W-31-109-Eng-38.

- ¹J. S. Kim, C. S. Johnson, and M. M. Thackeray, *Electrochem. Commun.* **4**, 492 (2002).
- ²T. Ohzuku, K. Ariyoshi, and S. J. Yamamoto, *J. Ceram. Soc. Jpn.* **110**, 501 (2002).
- ³T. Ohzuku, K. Ariyoshi, S. Yamamoto, and Y. Makimura, *Chem. Lett.* **1**, 1270 (2001).
- ⁴J. M. Paulsen, C. L. Thomas, and J. R. Dahn, *J. Electrochem. Soc.* **147**, 861 (2000).
- ⁵K. M. Shaju, G. V. Subba Rao, and B. V. R. Chowdari, *Electrochem. Commun.* **4**, 633 (2002).
- ⁶Z. Lu, L. Y. Beaulieu, R. A. Donabarger, C. L. Thomas, and J. R. Dahn, *J. Electrochem. Soc.* **149**, A778 (2002).
- ⁷Z. Lu and J. R. Dahn, *J. Electrochem. Soc.* **149**, A815 (2002).
- ⁸T. Ohzuku and Y. Makimura, *Chem. Lett.* **30**, 642 (2001).
- ⁹K. M. Shaju, G. V. Subba Rao, and B. V. R. Chowdari, *Electrochim. Acta* **48**, 145 (2002).
- ¹⁰Z. Lu, D. D. MacNeil, and J. R. Dahn, *Electrochem. Solid-State Lett.* **4**, A200 (2001).
- ¹¹D. D. MacNeil, Z. Lu, and J. R. Dahn, *J. Electrochem. Soc.* **149**, A1332 (2002).
- ¹²Y. Makimura and T. Ohzuku, *J. Power Sources* **119–121**, 156 (2003).
- ¹³T. Ohzuku and Y. Makimura, *Chem. Lett.* **1**, 744 (2001).
- ¹⁴T. Ohzuku, A. Ueda, and M. Nagayama, *Solid State Ionics* **67**, 123 (1993).
- ¹⁵G. Amucci, A. Du Pasquier, A. Blyr, T. Zheng, and J. M. Tarascon, *Electrochim. Acta* **45**, 255 (1999).
- ¹⁶E. Rossen, C. D. W. Jones, and J. R. Dahn, *Solid State Ionics* **57**, 311

- (1992).
- ¹⁷M. E. Spahr, P. Novak, O. Haas, and R. J. Nesper, *J. Power Sources* **68**, 629 (1997).
- ¹⁸J. S. Kim, C. S. Johnson, and M. M. Thackeray, *Electrochem. Commun.* **4**, 205 (2002).
- ¹⁹A. Deb, U. Bergmann, S. P. Cramer, and E. J. Cairns, *J. Appl. Phys.* **97**, 113523 (2005).
- ²⁰W.-S. Yoon, C. P. Grey, M. Balasubramanian, X.-Q. Yang, and J. McBreen, *Chem. Mater.* **15**, 3161 (2003).
- ²¹S. H. Na, S. H. Kim, and I. S. Moon, *Electrochim. Acta* **50**, 449 (2004).
- ²²K. M. Shaju, G. V. Subba Rao, and B. V. R. Chowdari, *Electrochim. Acta* **48**, 1505 (2003).
- ²³A. Deb, U. Bergmann, E. J. Cairns, and S. P. Cramer, *J. Synchrotron Radiat.* **11**, 497 (2004).
- ²⁴G. N. George and I. J. Pickering, *EXAFSPAK: A Suite of Computer Programs for Analysis of X-ray Absorption Spectra* (SSRL, 1993).
- ²⁵M. J. Newville, *J. Synchrotron Radiat.* **8**, 322 (2001).
- ²⁶H. Kobayashi, H. Sakaebe, H. Kageyama, K. Tatsumi, Y. Arachi, and T. Kamiyama, *J. Mater. Chem.* **13**, 590 (2003).
- ²⁷Y. Gao, M. V. Yakovleva, and W. B. Ebner, *Electrochem. Solid-State Lett.* **1**, 117 (1998).
- ²⁸J. R. Neuhaus-Mueller, R. A. Dunlap, and J. R. Dahn, *J. Electrochem. Soc.* **147**, 3598 (2000).
- ²⁹J. Reed and G. Ceder, *Electrochem. Solid-State Lett.* **5**, A145 (2002).
- ³⁰X. Q. Yang, J. McBreen, Y. S. Yoon, and C. P. Grey, *Electrochem. Commun.* **4**, 649 (2002).
- ³¹S. Sugano, Y. Tanabe, and H. Kamimura, *Multiplets of Transition-Metal Ions* (Academic, New York, 1970), Vol. 1, p. 73.
- ³²J. S. Griffith, *The Theory of Transition Metal Ions* (Cambridge University Press, Cambridge, 1961).
- ³³J. E. Hahn, A. Scott, K. O. Hodgson, S. Doniach, S. R. Desjardins, and E. I. Solomon, *Chem. Phys. Lett.* **88**, 595 (1982).
- ³⁴M. Belli, A. Scafati, A. Bianconi, S. Mobilio, L. Palladino, A. Reale, and E. Burattini, *Solid State Commun.* **35**, 355 (1980); A. Manceau, A. I. Gorskov, and V. A. Drits, *Am. Mineral.* **77**, 1133 (1992).
- ³⁵C. R. Horne, U. Bergmann, M. M. Grush, R. C. C. Perera, D. L. Ederer, T. A. Callcott, E. J. Cairns, and S. P. Cramer, *J. Phys. Chem. B* **104**, 9587 (2000).
- ³⁶G. J. Colpas, M. J. Maroney, C. Bagyinka, M. Kumar, W. S. Willis, S. L. Suib, N. Baidya, and P. K. Mascharak, *Inorg. Chem.* **30**, 920 (1991).
- ³⁷M. G. Kim, Y. S. Im, E. J. Oh, K. H. Kim, and C. H. Yo, *Physica B* **229**, 338 (1997).
- ³⁸A. Chainani, M. Mathew, and D. D. Sharma, *Phys. Rev. B* **46**, 9976 (1992).
- ³⁹A. Rougier, C. Delmas, and A. V. Chadwick, *Solid State Commun.* **94**, 123 (1995).
- ⁴⁰I. Nakai and T. Nakagome, *Electrochem. Solid-State Lett.* **1**, 259 (1998).
- ⁴¹Z. Lu and J. R. Dahn, *J. Electrochem. Soc.* **149**, A815 (2002).
- ⁴²T. W. Capehart, D. A. Corrigan, R. S. Conell, K. I. Pandya, and R. W. Hoffman, *Appl. Phys. Lett.* **58**, 865 (1991).
- ⁴³A. N. Mansour and C. A. Melendres, *J. Phys. Chem. A* **102**, 65 (1998).
- ⁴⁴R. D. Shannon, *Acta Crystallogr., Sect. A: Cryst. Phys., Diffraction, Theor. Gen. Crystallogr.* **32**, 751 (1976).
- ⁴⁵A. N. Mansour, J. McBreen, and C. A. Melendres, *J. Electrochem. Soc.* **146**, 2799 (1999).
- ⁴⁶W. E. O'Grady, K. I. Pandya, K. E. Swider, and D. A. Corrigan, *J. Electrochem. Soc.* **143**, 1613 (1996).
- ⁴⁷J. M. Kim and H. T. Chung, *Electrochim. Acta* **49**, 3573 (2004).